Numerical Methods in Civil Engineering, 10-3 (2026) 109-123

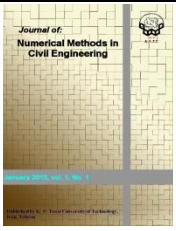

Numerical Methods in Civil Engineering

Journal Homepage: https://nmce.kntu.ac.ir/

Delamination Detection by Numerical Modelling of End-Notched Flexure Tests on glass/epoxy composite beams.

Mahdieh Sabbaghian*, Mohammad Zaman Kabir, Morteza Amooie*****

ARTICLE INFO

RESEARCH PAPER

Article history:
Received:
February 2026
Revised:
June 2026
Accepted:
July 2026

Keywords:
Strain energy release rate, Finite element, Mode II interlaminar fracture toughness, Composite materials, End-notched flexure, Virtual crack closing method.

Abstract:

The detection of delamination is important in structural engineering applications for assessing the reliability of fiber-reinforced polymer (FRP) laminates, which could provide appreciable effects on the behavior of composite structures. Numerical investigation of interlaminar shear fracture (Mode II) was studied in the present work by the end-notched flexure (ENF) testing configuration. 20 glass/epoxy composite beams were analyzed with two different stacking sequences, incorporating four distinct stacking sequences with different fiber orientation angles and five initial crack lengths (a = 35, 40, 45, 50, and 55 mm). Finite element analysis was performed using ABAQUS, and the virtual crack closure technique (VCCT) was used to determine the distribution of the critical strain energy release rate with respect to the width of the laminate. The results obtained were then analyzed using a subsequent finite element analysis of interlaminar stresses in the area ahead of the crack tip. The results from the numerical analysis showed that the dominant contribution to the total energy release rate was the mode II (G_{II} > 99%). Furthermore, the variation in G_{II} across the laminate width was almost unchanged. For the other nodes, however, near the free edges, the separation of the node pairs, combined with the need to meet the fracture criterion, resulted in significant shear effects, with mode III components (G_{III}) becoming comparable to G_{II}.

1. Introduction

Carbon fiber-reinforced polymer (CFRP) laminates have been used widely across various engineering fields such as aerospace, automotive, marine, civil, mechanical, and energy structures, owing to their high specific strength, high stiffness-to-weight ratio, corrosion resistance, and design flexibility [1,2]. However, several damage mechanisms can occur in composite laminates, and matrix cracking and delamination are the most significant. Delamination, caused by the propagation of interlaminar cracks, is a major cause of loss of stiffness and load-carrying capacity in the structure and can even result in catastrophic failure [3,4].

* *Corresponding author, Ph.D. Candidate, Department of Civil and Environmental Engineering, Amirkabir University of Technology (Tehran Polytechnic), Tehran, Iran. Email: Sabbaghian@aut.ac.ir.*
** *Professor, Department of Civil and Environmental Engineering, Amirkabir University of Technology (Tehran Polytechnic), Tehran, Iran. Email: mzkabir@aut.ac.ir.*
*** *Ph.D., Department of Civil Engineering, Guilan University, Guilan, Iran. Email: amooie@phd.guilan.ac.ir.*

Both the interfacial properties and characteristics between adjacent plies and matrix properties play an important role in the initiation and growth of delamination. Therefore, delamination can occur as a result of matrix brittleness, impact loading, stress concentrations at free edges and joints, high interlaminar stresses, fatigue damage and manufacturing defects. Numerous research has consequently been directed towards understanding and predicting delamination behavior in laminated composite structures [5,6]. Two commonly used methods to delamination analysis are fracture mechanics and cohesive zone modeling. The fracture mechanics approach characterizes crack propagation using the strain energy release rate (ERR), which represents the energy available for crack growth. Delamination may occur under three basic modes of fracture, namely opening mode (Mode I), sliding mode (Mode II), tearing mode (Mode III) and mixed mode (Modes I, II, and III) [7–9].

https://doi.org/10.61882/NMCE.2602.1126

Mode I and Mode II loading critical strain energy release rates are typically determined through standard experimental methods such as double cantilever beam (DCB) testing and end-notched flexure (ENF) testing, respectively [10,11].

During crack propagation under general loading conditions, in homogeneous isotropic materials, cracks tend to change orientation to ensure that the crack tip is mainly under Mode I loading. Delamination in laminated composites, however, is limited to propagating in relatively weak interlaminar interfaces. Therefore, crack growth often takes place under mixed mode conditions where all three modes (Modes I, II and III) are involved simultaneously. Griffith's energy-based fracture theory states that a fracture occurs when the strain energy release rate (G) equals the critical value of the strain energy release rate (G_c) which represents the material's resistance to fracture. Therefore, the accurate determination of the critical fracture toughness values becomes essential for the reliable evaluation and design of composite structures under complex loading conditions [12].

Numerous experimental studies have been conducted to investigate the interlaminar fracture performance of composite laminates under Mode I and Mode II loading conditions. Among the earliest investigations, Bascom et al. [13] demonstrated the beneficial effect of matrix toughening on the interlaminar fracture resistance of woven composite systems. To explore the Mode II delamination properties of stitched woven CFRP laminates, Wood et al. [14] carried out an experimental study on ENF specimens and emphasised the influence of fiber bridging on the fracture resistance of the laminate. Similarly, Alif et al. [15] investigated the interlaminar fracture of woven carbon/epoxy under Mode I, Mode II and Mixed-Mode loading and provided valuable insights into crack initiation and propagation mechanisms in these two different modes.

While relatively stable crack propagation behavior makes unidirectional (UD) laminates useful for interlaminar fracture characterization for practical engineering structures, a more typical structure will be made up of multidirectional (MD) laminate configurations. Delamination in these laminates occurs between plies of different fiber orientations causing more complicated fracture mechanisms. Pereira and de Morais [16] experimentally studied the interlaminar fracture toughness of multidirectional glass/epoxy laminate and showed that laminate configuration plays a significant role in the interlaminar fracture resistance. The same result has been reported by Triki et al. [17] who investigated the fracture toughness of woven composite laminates as a function of ply orientation. Recently, Gliszczynski and Wiącek [18] carried out a thorough experimental and numerical benchmark study using ENF testing and validated the reliability of currently used fracture characterization procedures to determine (G_{II_c}). In addition, Gong et al. [19] have developed a semi-analytical model to predict the Mode II fracture toughness of multidirectional CFRP laminates and shown that the interfacial ply angles have significant effects on the development of matrix damage and crack migration mechanisms, affecting the fracture resistance. Recently, Tu et al. [20] conducted a comparative study of the Mode II delamination properties of multidirectional and unidirectional laminates and found significant variation in delamination properties for different stacking sequences, especially when assessing the structural integrity of the laminated structures.

Although a lot of research has been carried out, it is still reported that the fracture toughness of Mode II and crack propagation mechanisms are highly dependent on material system, laminate architecture and loading conditions. The effect of ply orientation on (G_{II_c}) was shown to have a non-linear effect in previous studies due to other interacting damage mechanisms such as fiber bridging, matrix cracking, crack migration, and other interacting damage mechanisms [21–24]. Recent studies, have also observed that material modifications can significantly affect Mode II fracture behaviour. Sarr and Kosaka [25] have observed that, when added to glass/epoxy laminates, cellulose nanofibers were found to increase the Mode II fracture toughness by the mechanisms of increased energy dissipation and crack-growth resistance. Abdullah et al. [26] studied Mode II and Mode III delamination in carbon/epoxy laminated plates under four-point bending loadings and revealed the effects of loading configuration on interlaminar fracture mechanisms. In addition, Gfrerrer et al. [27] compared Mode I, Mode II and mixed Mode interlaminar fracture toughness of two types of glass and carbon fiber reinforced polymer composites produced with the same epoxy matrix system and showed that fiber architecture and type of reinforcement are still important parameters that influence delamination resistance.

Numerous studies have provided valuable information on the Mode II delamination of composite laminates; however, several major issues remain unresolved. Despite the high number of investigations available, little work has been performed so far to understand how laminate stacking sequence and initial crack length influence the 3-D distribution of strain energy release rate in multidirectional woven composite laminates. Moreover, the role of anticlastic deformation and Mode III edge effects has not yet been completely understood. The main objective of the present study is to explore the Mode II delamination behavior of thick woven glass/epoxy laminates by conducting a detailed numerical study. Firstly, the previously published experimental results are reproduced and validated. The influence of laminate stacking sequence and initial crack length on the critical SERR is then studied via a parametric study. The three dimensional distribution of fracture parameters within the specimen width is highlighted, and attention is given to the effect of edge induced mixed mode fracture. The results give a better understanding of the mechanism of delamination of multidirectional composite laminate and can be used for the design of composite structures with better resistance to interlaminar failure.

2. FE Modelling of ENF Specimens

The simulation of these glass/epoxy composite laminates was carried out in Abaqus/CAE, which offers specific features for the crack propagation analysis using the linear elastic fracture mechanics (LEFM)–based VCCT. Evaluation of delamination growth in multilayered materials in a fracture mechanics context is possible using the VCCT approach. This approach is based on LEFM concepts in order to determine the energy released from the crack propagation as the crack moves between the layers, thereby enabling the accurate prediction of interlaminar failure [28–35].

2.1 Laminate Layup Configuration

Mechanical coupling must be avoided when evaluating G_{II_c} for multidirectional laminates, and the layup configuration must be chosen to ensure this. Unless controlled, flexural coupling phenomena can lead to significant anticlastic responses and accordingly to a significant non-planar delamination path, and maybe even to an unwanted mode III component, especially along the specimen boundaries [21,22,24,36–38].

Therefore, Davidson et al. suggested restricting the value of the bending stiffness parameter D_c by means of the criteria described in Eq. (1) [37].

In addition, if the starter crack occurs at an interface between plies of different ply orientations, further coupling effects can arise and affect the fracture response, such as flexure–torsion interaction and in-plane/bending coupling. These interactions can create non-symmetric crack fronts and can greatly magnify the effect of residual stresses on the apparent fracture toughness. MD configurations typically have lower stiffness than unidirectional laminates, but can have higher fracture resistance [39]. Therefore, thicker specimens are preferred, when possible, to prevent excessive displacements, plasticity and internal damage in the specimen during testing. This led to the following stacking sequence being chosen for this study, as shown in Figure 1. To facilitate description the specimens are referred to briefly as *S1*, *S2*, *S3* and *S4*.

$$\boldsymbol{D_c = \frac{D_{12}^2}{D_{11}D_{22}} \leq 0.25} \quad (1)$$

1. *S1*: $[(0_2/90)_6/0_2//\ (0_2/90)_6/0_2]$ consist of 40 plies.
2. *S2*: $[(0_2/90)_6/0_2//45/\ (0_2/90)_6/0_2]$ consist of 41 plies.
3. *S3*: $[(0_2/90)_6/0_2//90/(0_2/90)_6/0_2)]$ consist of 41 plies.
4. *S4*: $[(0_2/90)_6/0_2/45//{-45}/\ (0_2/90)_6/0_2]$ consist of 42 plies.

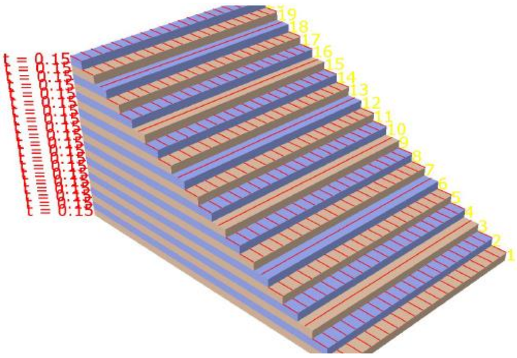

S1: $[(0_2/90)_6/0_2//\ (0_2/90)_6/0_2]$

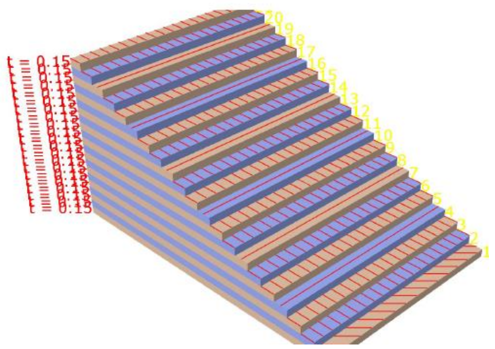

S2: $[(0_2/90)_6/0_2//45/\ (0_2/90)_6/0_2]$

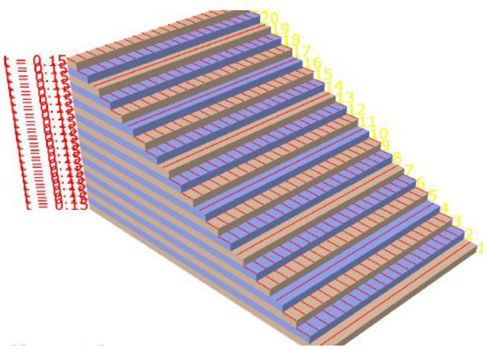

S3: $[(0_2/90)_6/0_2//90/(0_2/90)_6/0_2)]$

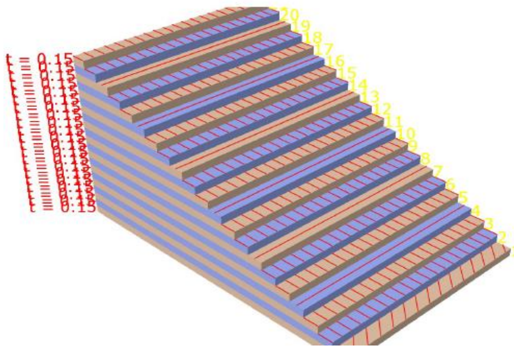

S4: $[(0_2/90)_6/0_2/45//{-45}/\ (0_2/90)_6/0_2]$

Fig. 1: The specimen stacking sequence

where // indicates the position of the starting delamination. Integrating the thick symmetric block $[(0_2/90)_6/0_2]$ of twenty plies aims to reduce the undesirable elastic couplings mentioned above.

2.2 FE Modeling of ENF specimens

The specimens were modelled in a 3-dimensional FE analysis [40,41]. According to the Figure. 2.a, the specimen dimensions are considered as: the total length 2L=160 mm, span length 100 mm, crack length *a* = (35, 40, 45, 50, 55) mm, and width *b* = 20 mm. The selected crack lengths (35–55 mm) correspond to an a/L ratio ranging from 0.44 to 0.69, which lies within the commonly accepted range for ENF testing to ensure stable crack propagation and comparable mode II-dominated fracture behavior. This range minimizes boundary-condition effects and preserves the validity of the strain energy release rate analysis. The thickness of each ply was equal to 0.15 mm; therefore, the laminate thickness *2h* is varied from 6.0 to 6.3 mm.

Although the total laminate thickness varied slightly among the studied configurations (6.0–6.3 mm), this variation remained below 5% and was considered negligible compared with the influence of fiber orientation and stacking sequence. Therefore, the observed differences in delamination behavior were primarily attributed to stacking sequence effects rather than thickness-related stiffness changes. The finite element models were developed using ABAQUS. The ENF fixture was modelled using three cylindrical rollers represented as discrete rigid surfaces. Two rollers acted as supports, and one acted as the central loading roller. Loading and boundary conditions were applied through reference points associated with the rigid rollers. Surface-to-surface contact was defined between the rollers and the specimen using hard contact in the normal direction and Coulomb friction with a coefficient of 0.2 in the tangential direction.

Figure. 2.b illustrates the finite element discretization adopted in the present study. The composite laminate was discretized using S4R shell elements, while R3D4 discrete rigid elements represented the loading and support rollers. A mesh sensitivity analysis was performed using global mesh sizes of 0.5, 1, 2, 3, and 4 mm. The calculated strain energy release rate values showed convergence with mesh refinement, and the differences between the 2mm, 1 mm, and 0.5 mm meshes were negligible. Therefore, a global mesh size of 2 mm was selected as an optimal balance between computational efficiency and numerical accuracy. In addition, local mesh refinement was applied in the crack-front region using a seed size of 0.1 mm to improve the accuracy of the VCCT calculations.

According to ASTM D7905 [42], the ENF specimen geometry and loading configuration adopted in this study included the standardized specimen dimensions, support span, three-point bending fixture arrangement, and predefined initial crack placement. Since the present work is exclusively numerical, experimental procedures such as preload application and physical data acquisition specified in ASTM D7905 [42] were not applicable. In addition, instead of using the standard experimental data-reduction method, the strain energy release rate components were directly calculated using the VCCT, which is more suitable for finite element fracture analysis.

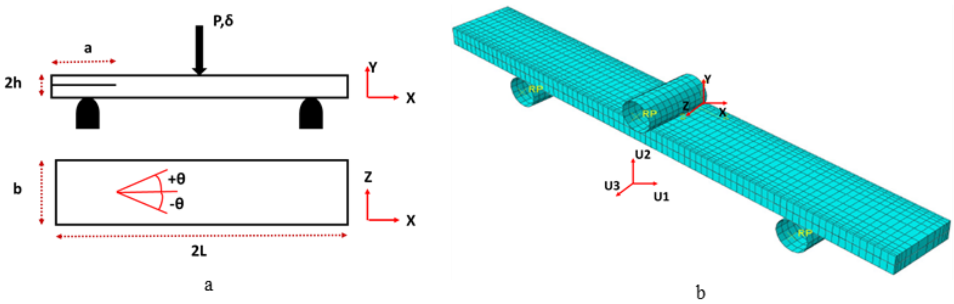

Fig. 2: a) ENF specimen schematic, b) Schematic FE mesh

For this research, 20 beam specimens were tested in accordance with the standard which is related to the testing of ENF specimens, and the specimen details are presented in Table 1.

A woven glass fibre–reinforced epoxy composite was used as the base material in this research for all specimens. Thermoelastic properties are presented as per Table 2. The orthotropic properties listed in Table 2 represent the homogenized equivalent properties of the woven glass/epoxy composite material rather than individual ply-level lamina properties. These equivalent material parameters were adopted from previously published literature and were used to model each woven ply as an orthotropic continuum in the finite element analysis. The woven glass/epoxy composite was modeled as a purely linear elastic orthotropic material using the elastic constants listed in Table 2. No plasticity or progressive damage model was considered, since the objective of the present work was to evaluate delamination initiation and early crack propagation under elastic loading conditions, for which the assumptions of linear elastic fracture mechanics (LEFM) and the applicability of VCCT remain valid.

Table 1: List of ENF specimens

[*S1*]- *a*=35	[*S2*]- *a*=35	[*S3*]- *a*=35	[*S4*]- *a*=35
[*S1*]- *a*=40	[*S2*]- *a*=40	[*S3*]- *a*=40	[*S4*]- *a*=40
[*S1*]- *a*=45	[*S2*]- *a*=45	[*S3*]- *a*=45	[*S4*]- *a*=45
[*S1*]- *a*=50	[*S2*]- *a*=50	[*S3*]- *a*=50	[*S4*]- *a*=50
[*S1*]- *a*=55	[*S2*]- *a*=55	[*S3*]- *a*=55	[*S4*]- *a*=55

Table 2: Glass-epoxy specifications

Material properties of undamaged layers					
E_1(MPa)	`$E_2 = E_3$(MPa)	ν23 = ν13	ν12	G13 = G23 (MPa)	G12(**MPa**)
33000	19000	0.17	0.46	3000	4800
Benzeggagh - Kenane (BK) crack propagation			**Fracture energies (N/mm)**		
BK (power)			G_{I_c}	G_{II_c}	$\mathbf{G_{III_c}}$
1.75			42.2	42.2	42.2

2.3 Virtual crack closure technique

The VCCT-based formulation for identifying the mode mixity in orthotropic composite delamination, illustrated in Figure 3, was applied to evaluate the contributions of the separate fracture energy components associated with modes I, II, and III. Previous studies have demonstrated that the stress distribution in the vicinity of a delamination located between plies with different orientations is highly non-uniform and may exhibit local oscillations, and that the apparent mode separation can be influenced by the assumed crack-closure increment [29,39,40]. However, Δa can be treated as a characteristic length of the damage zone that has a value similar to the ply thickness. When interpreted in this manner, the partitioning of fracture modes becomes essentially stable and less sensitive to numerical assumptions. In the present analysis, the results were obtained by adopting Δa = t/2, which provides a consistent representation of the energy release rate components [40].

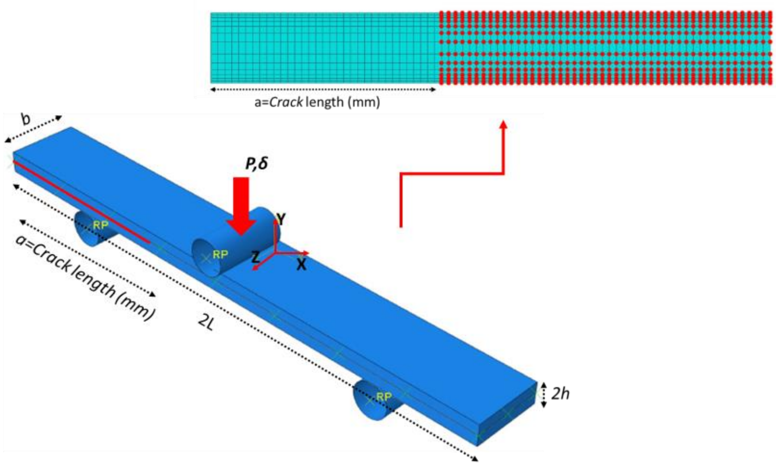

Fig. 3: Virtual crack closure technique (VCCT)

3. Results of FE modelling

In this part, the finite element results obtained from the benchmark ENF configuration proposed by Pereira et al. [16] are presented and discussed. The finite element model was developed based on the benchmark ENF configuration reported by Pereira et al. [16]. It should be noted that the objective of the present study is not to perform a direct validation against the original experimental dataset, but rather to investigate the effects of stacking sequence and initial crack length on the strain energy release rate behavior. Owing to differences in modeling assumptions, material characterization, and response parameters considered in the present analysis, a direct quantitative comparison with the experimental results of Pereira et al. was not pursued. Instead, the adopted modeling approach was assessed through its ability to reproduce the overall mechanical behavior and fracture characteristics reported in the reference study.

Figure 4 shows the stress distribution (Von Mises), Figure 5, 6, indicate the stress distribution along S22 and S12, and Figure 7, 8, and 9 depict the displacement distribution in the directions U1, U2, and U3, respectively, for specimens with the initial notch length of *a*=45 mm and stacking sequence configuration of *S1*.

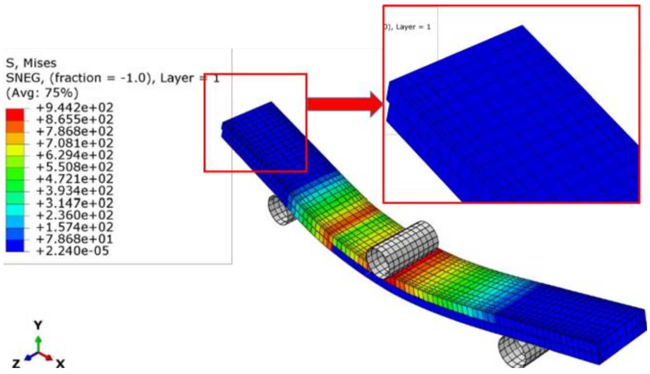

Fig. 4: Von-Mises stress distribution of specimen *S1* with an initial crack length of *a* = 45 mm.

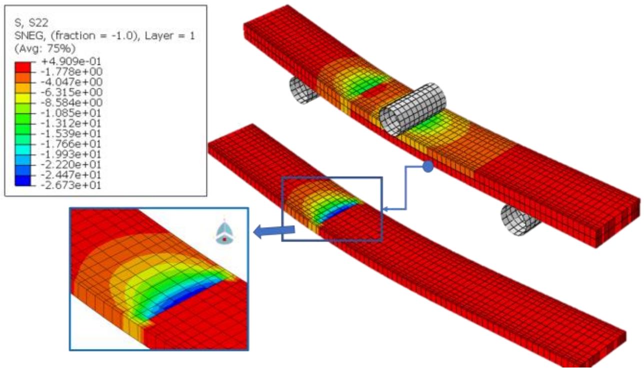

Fig. 5: stress distribution along S22 of specimen *S1* with an initial crack length of *a* = 45 mm.

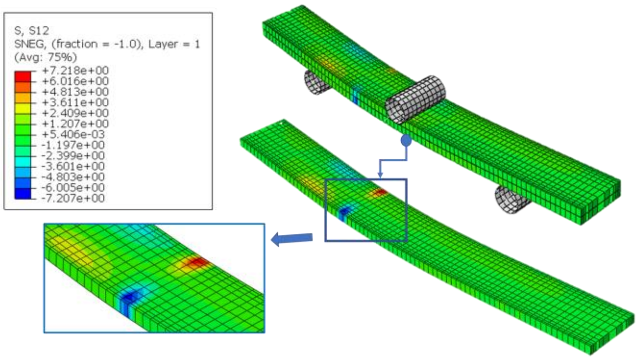

Fig. 6: stress distribution along S12 of specimen *S1* with an initial crack length of *a* = 45 mm.

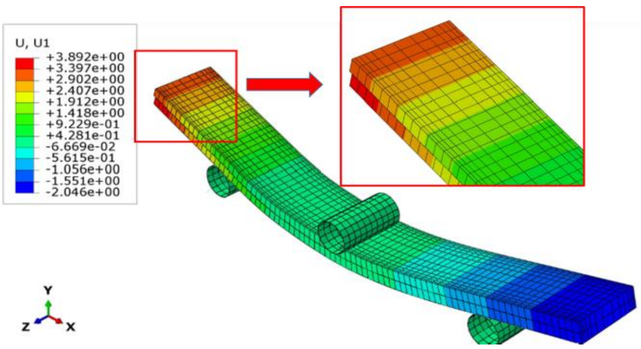

Fig. 7: Displacement distribution along U1 of specimen *S1* with an initial crack length of *a* = 45 mm.

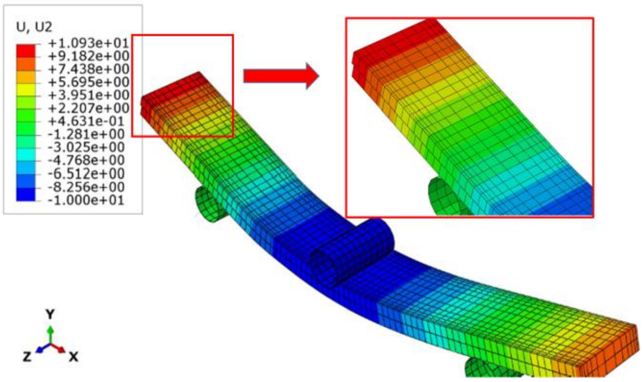

Fig. 8: Displacement distribution along U2 of specimen *S1* with an initial crack length of *a* = 45 mm.

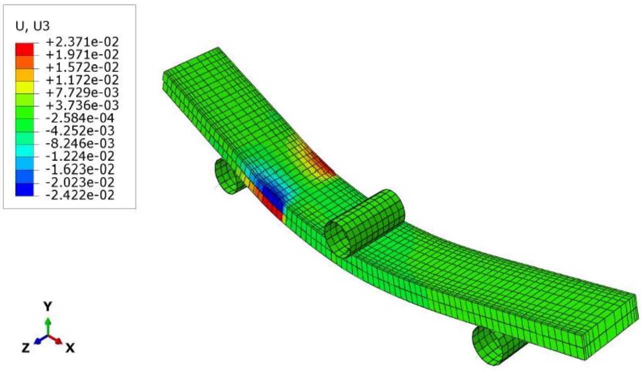

Fig. 9: Displacement distribution along U3 of specimen *S1* with an initial crack length of *a* = 45 mm.

To determine G values, only the lower part of the model in Abaqus was activated. The whole strain energy is measured by Eq (2) .Where G_I, G_{II}, and G_{III} are the mode I (opening mode), II (sliding mode), and III strain (tearing mode) energy. The distribution of G across the width of the ENF specimen with the stacking sequence of S_1 and *a*=45 mm is according to Figure 10. The strain energy release rate values of G_I, G_{II}, and G_{III}, the sum of G and the normalized values of G in different directions, which are the ratio of G in each mode to the average G in the same mode, and then the ratio of G_{II} /G of the ENF specimen with stacking sequence of S_1 and *a*=45 mm, are presented in Table 3. Also, the strain energy release rate curves of G_I, G_{II}, and G_{III}, and the sum of G, are shown in Figure 11. The normalized values of G in different directions, i.e., the ratio of G in each mode (mode I, II, III, and total) to the average G in the same mode are depicted according to Figure 12. The ratio of G_{II} /G across the width of the specimen is illustrated in Figure 13. The results showed that the distributions of G_I, G_{II}, and G_{III} along the width of the ENF specimen with the stacking sequence of S_1 and *a*=45 mm apart from the local edge effects are completely uniform. In addition, the results of Figure 13 and Table 3 confirmed the high percentage of mode II, the average mode II component in the ENF specimen with a stacking sequence of *S1* and *a*=45 mm above 99% of the total release rate. According to plots, the value of G_{III} is negligible through the laminate width, but at the edges, the value of strain energy in mode III is comparable to G_{II} due to splitting of the front delamination's node pairs according to fulfilling the fracture criterion ($G \geq G_c$). In fact, it is the boundary effect that is confirmed by curves related to the G_{III}. This phenomenon shows strong shearing effects at the boundaries regardless of the type of stacking sequence and fiber orientation, confirming the combination of modes II and III in the edges according to Samborski [43] and the effect of anticlastic occurrence at the edges [43].

$$G = G_I + G_{II} + G_{III} \quad (2)$$

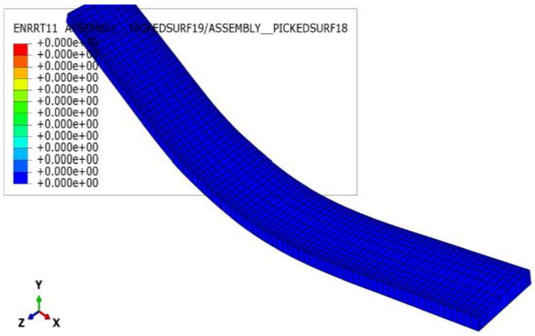

G_I distribution

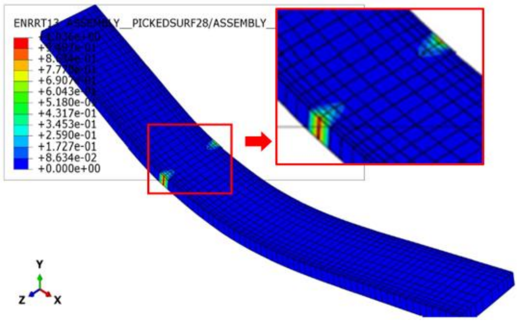

G_{III} distribution

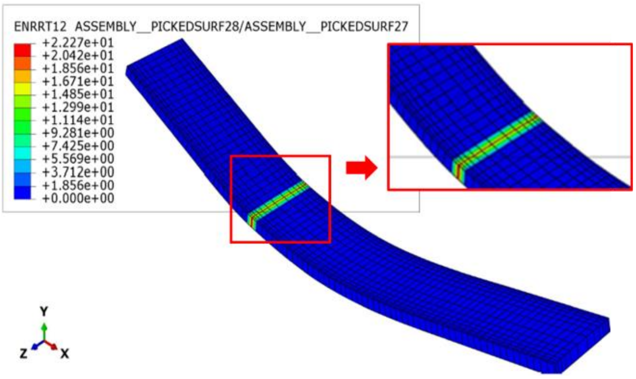

G_{II} distribution

Fig. 10: Distribution of different strain energy across the width of the specimen with *S1* and *a*=45mm

Table 3: G values in the width of the specimen with *S1* and *a*=45mm

Y	G1	G2	G3	G1 (Normalized)	G2 (Normalized)	G3 (Normalized)	Gt	G2/Gt
0	0.00	22.27	1.03	0.00	1.19	3.49	23.31	0.96
0.576	0.00	18.51	0.45	0.00	0.99	1.52	18.96	0.98
1.352	0.00	17.88	0.29	0.00	0.96	0.98	18.17	0.98
2.398	0.00	17.92	0.18	0.00	0.96	0.59	18.10	0.99
3.809	0.00	18.04	0.09	0.00	0.96	0.30	18.13	1.00
5.710	0.00	18.13	0.03	0.00	0.97	0.11	18.16	1.00
8.273	0.00	18.16	0.00	0.00	0.97	0.01	18.17	1.00
11.727	0.00	18.16	0.00	0.00	0.97	0.01	18.17	1.00
14.290	0.00	18.12	0.03	0.00	0.97	0.11	18.16	1.00
16.191	0.00	18.04	0.09	0.00	0.96	0.30	18.13	1.00
17.602	0.00	17.91	0.18	0.00	0.96	0.59	18.09	0.99
18.648	0.00	17.87	0.29	0.00	0.96	0.98	18.16	0.98
19.424	0.00	18.50	0.45	0.00	0.99	1.52	18.95	0.98
20.000	0.00	22.27	1.04	0.00	1.19	3.49	23.31	0.96
average	0.00	18.70	0.30				19.00	0.99

*Y: Width of Laminate (mm)
*G1, G2, G3: Strain energy release rate components mJ/mm^3
*G1, G2, G3 (Normalized): Normalized strain energy release rate components
*Gt (Total)= G1+G2+G3

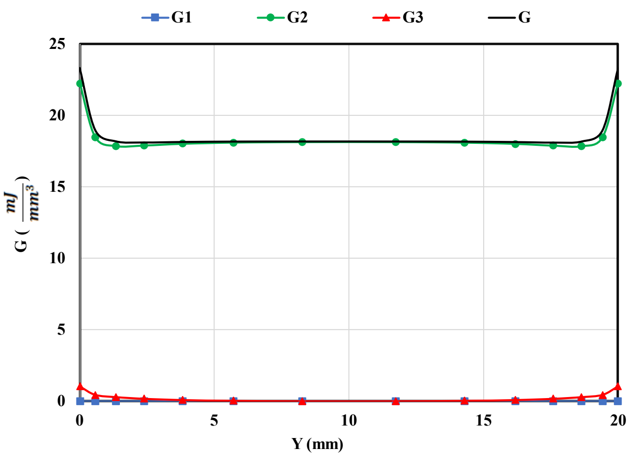

Fig. 11: G-Y curve across the width of the specimen with *S1* and *a*=45mm

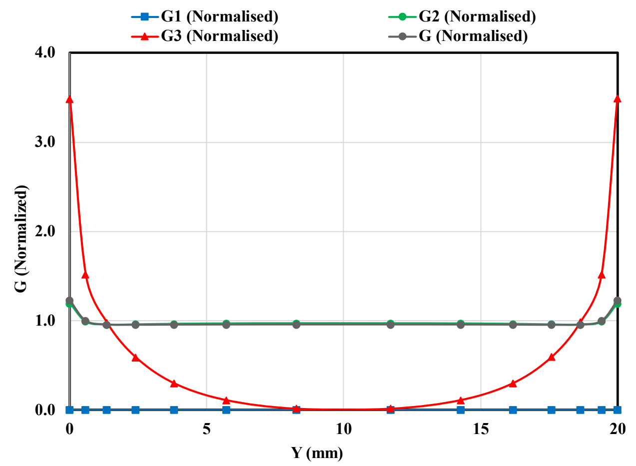

Fig. 12: $G_{[Normalised]}$-Y curve across the width of the specimen with *S1* and *a*=45mm

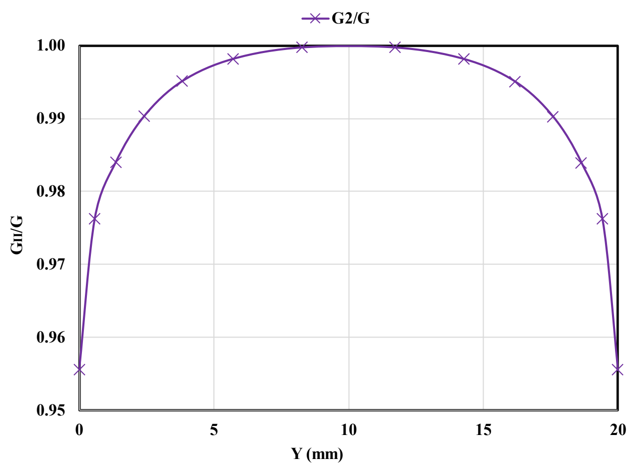

Fig. 13: G_{II} /G curve across the width of the specimen with *S1* and *a*=45mm

To verify that the increase in G_{III} near the free edges was not a numerical artifact, a mesh sensitivity analysis was conducted using global mesh sizes of 0.5, 1, 2, 3, and 4 mm together with local crack-front refinement. The widthwise distributions of G_{II} and G_{III} remained essentially unchanged after mesh refinement, confirming mesh-independent results. In addition, the symmetric distribution of GIII with localized peaks at both free edges was consistently observed for all mesh densities, indicating that the observed behavior is associated with free-edge effects and anticlastic deformation rather than VCCT node-pairing or mesh distortion artifacts.

3.1 The effect of initial crack length on G values (in fixed stacking sequence)

3.1.1 Effect of initial crack length on G_I

Table 3 shows that the values of G_I were approximately zero (smaller than (e-12)); therefore, its investigation has been neglected.

3.1.2 Effect of initial crack length on G_{II}

Comparison of G_{II} values across the width of the ENF specimen for the first stacking sequence of *S1*, the second stacking sequence of *S2*, the third stacking sequence of *S3,* and the fourth stacking sequence of *S4* is according to Figures 14. The results showed that as the initial crack length increased, the strain energy release rate in the specimen also increased; therefore, the tendency of separation of the plies increases in cases where the length of the initial crack is longer.

3.1.3 Effect of initial crack length on G_{III}

Comparison of G_{III} values across the width of the ENF specimen for the first stacking sequence of S1, the second stacking sequence of S2, the third stacking sequence of S3, and the fourth stacking sequence of S4 is according to Figures 15. The results showed that the values of G_{III} in the middle part of all the specimens were zero, but at the edges of the beam, with the increase in the length of the initial crack, the values of the strain energy release rate in the specimen increase, and therefore the tendency of separation of layers increases in cases where the length of the initial crack is longer at the edges.

3.2 Effect of the stacking sequence on G

3.2.1 Effect of the stacking sequence on G_I

Table 3 shows that the G_I values were smaller than (e-12) therefore it can be considered zero.

3.2.2 Effect of the stacking sequence on G_{II}

Comparison of G_{II} values and G_{II} /G values in the width of ENF specimen for the initial crack length *a*=35 mm, *a*=40 mm, *a*=45 mm, *a*=50 mm, and *a*=55 mm, respectively, according to Figures 16 to 20.

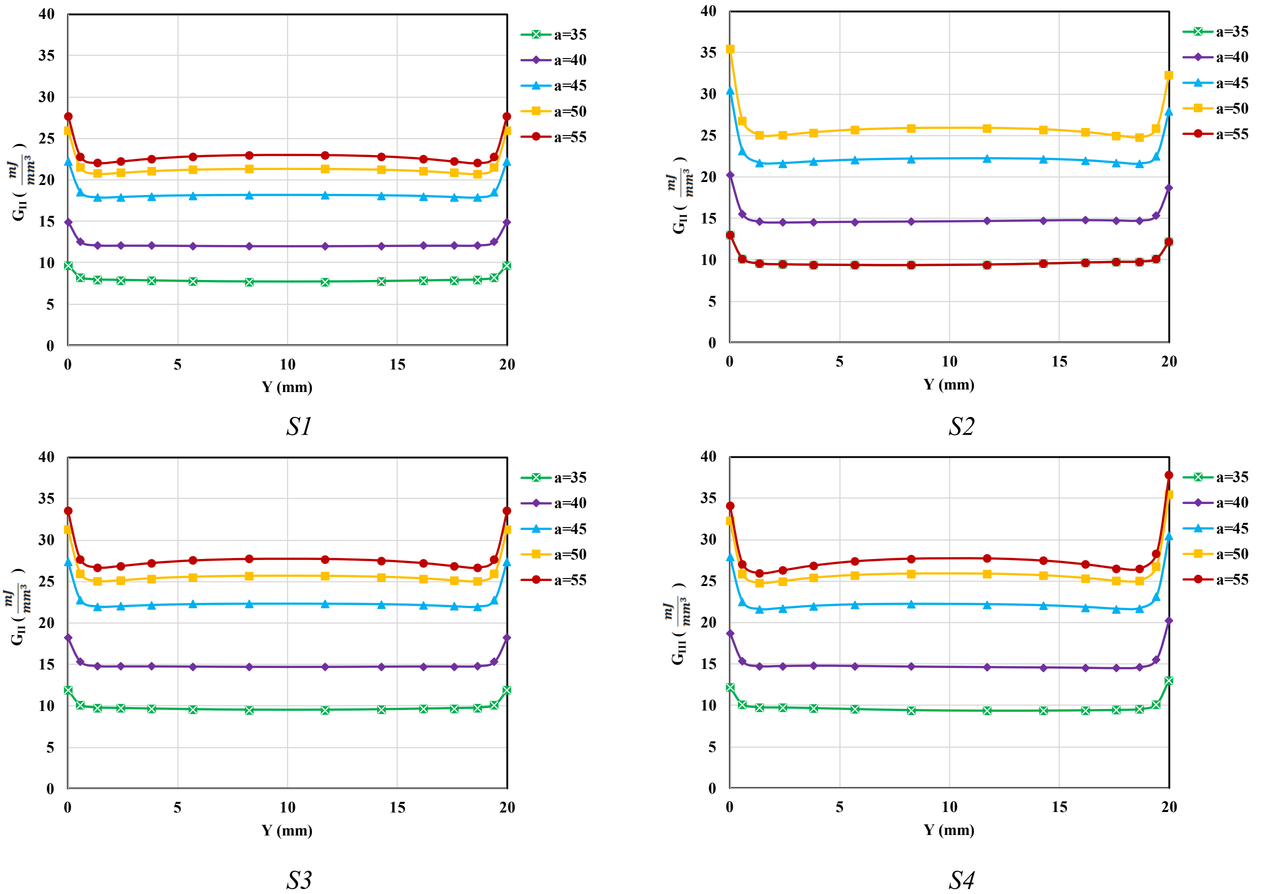

Fig. 14: Comparison of G_{II} values across the specimen's width according to fixed stacking sequence

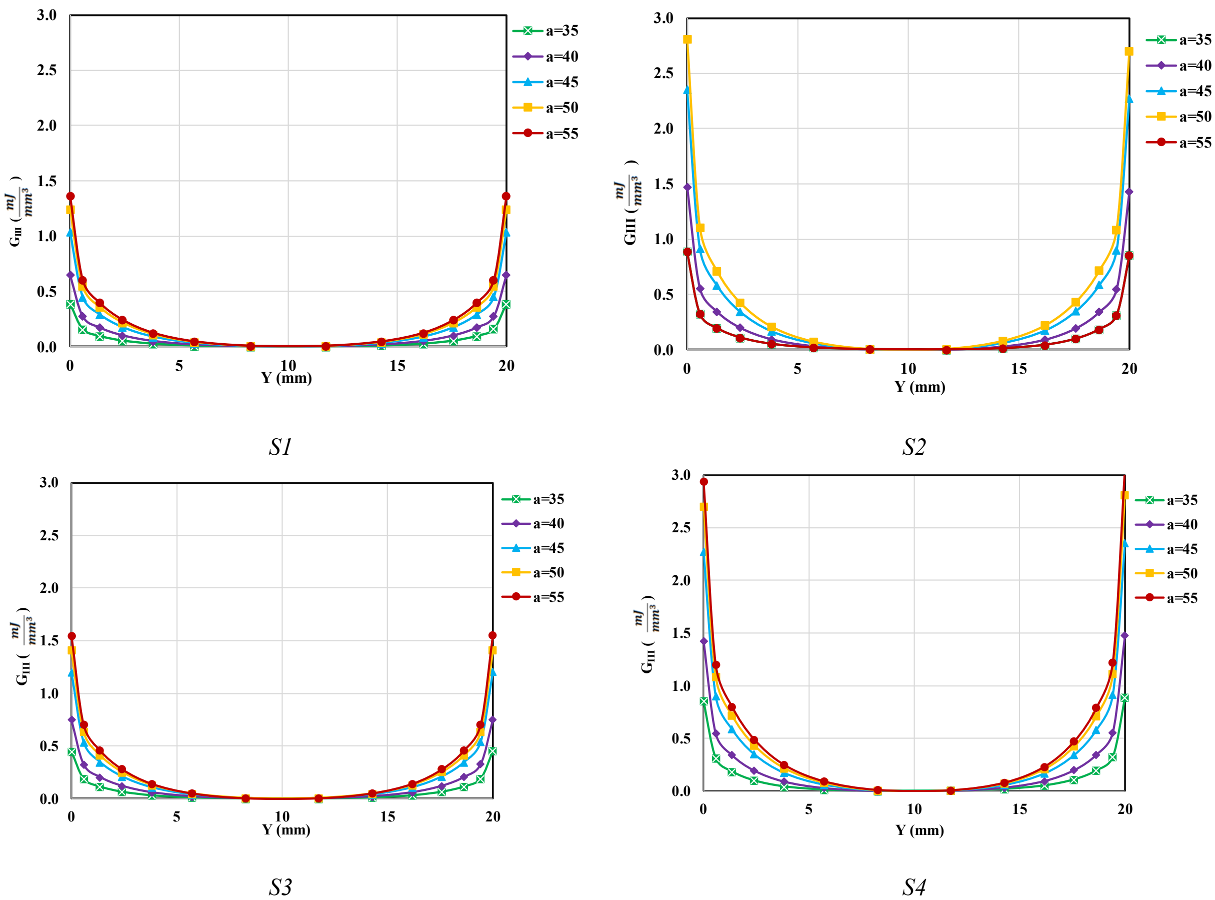

Fig. 15: Comparison of G_{III} values across the specimen's width according to fixed stacking

The results showed that with the change of the stacking sequence, the values of the strain energy release rate in the specimen change, according to the mentioned curves, the value of the energy release rate is the lowest in *S1,* and with the asymmetry of the stacking sequence of *S2* and *S3*) or angling the fibers (*S4*), The available G_{II} values are increased and therefore the possibility of delamination increases in these cases.

From a fracture mechanics viewpoint, the strain energy release rate represents the energy available for crack extension per unit increase in delaminated area. Therefore, an increase in G_{II} indicates a greater driving force for interlaminar crack propagation. Since the ENF configuration generates predominantly interlaminar shear stresses ahead of the crack tip, the delamination process is governed mainly by mode II fracture. Consequently, the higher G_{II} values observed for asymmetric stacking sequences (*S2* and *S3*) and angled interfaces (*S4*) imply a greater tendency for crack growth, whereas the lower G_{II} values obtained for *S1* indicate improved resistance to delamination propagation.

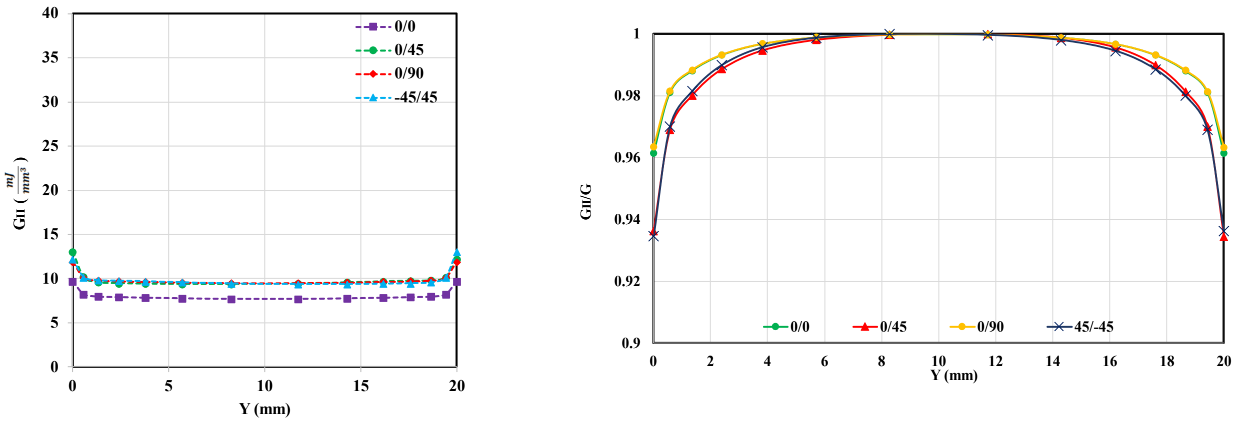

a b

Fig. 16: Comparison of values in ENF specimen width for *a*=35 mm a) G_{II} values b) G_{II} /G values

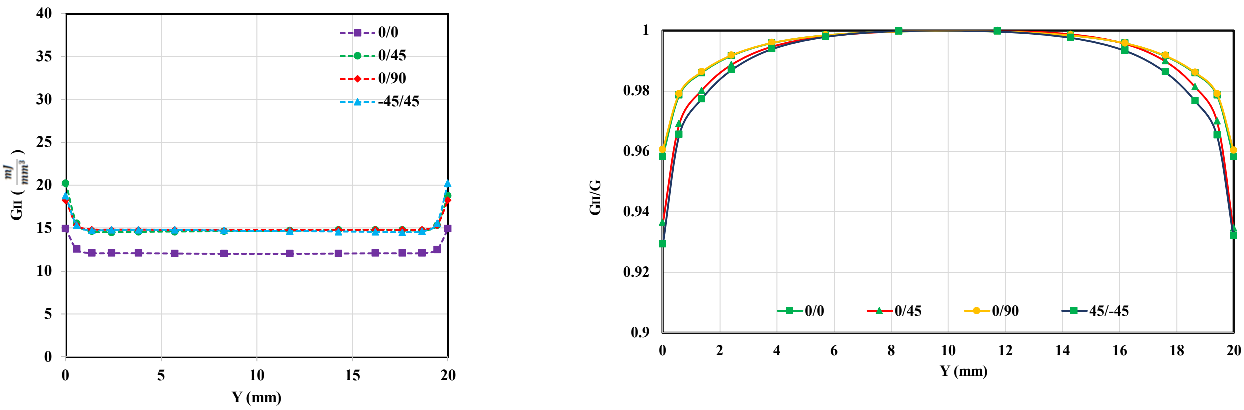

a b

Fig. 17: Comparison of values in ENF specimen width for *a*=40 mm a) G_{II} value b) G_{II} /G values

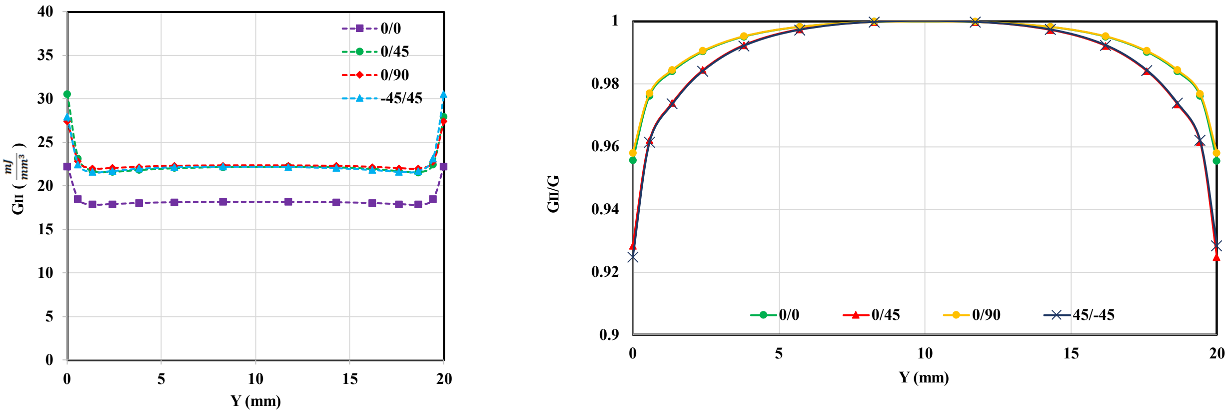

a b

Fig. 18: Comparison of values in ENF specimen width for *a*=45 mm a) G_{II} values b) G_{II} /G values

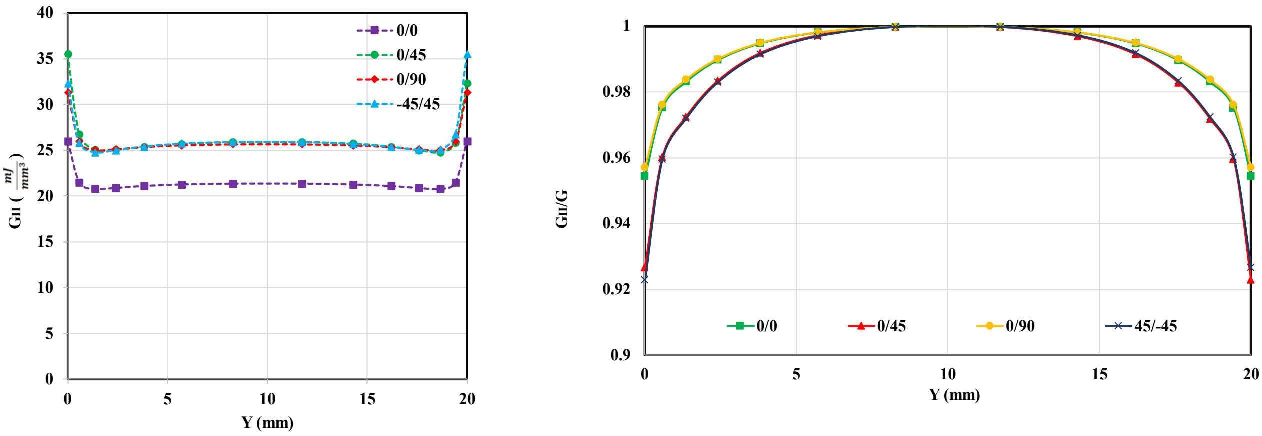

a b

Fig. 19: Comparison of values in ENF specimen width for *a*=50 mm a) G_{II} values b) G_{II} /G values

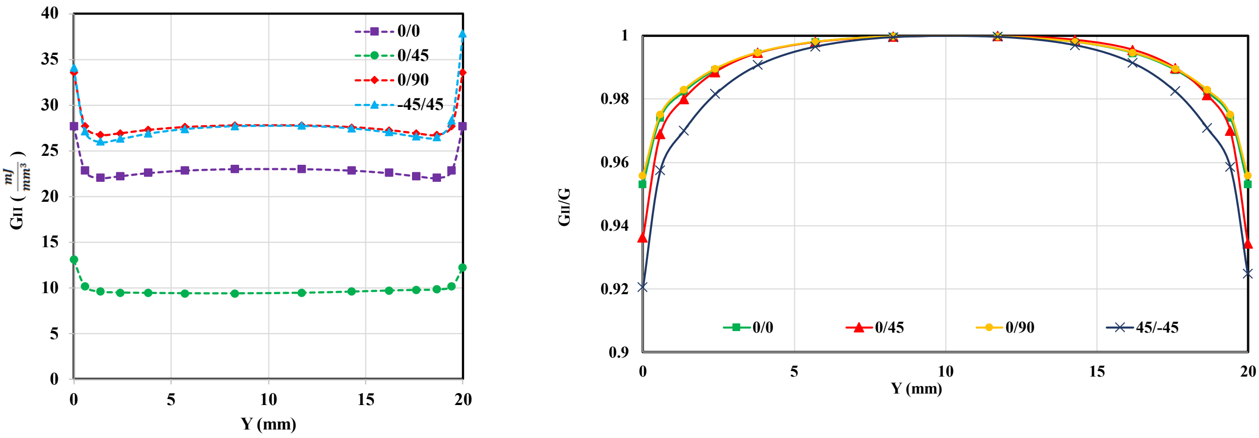

a b

Fig. 20: Comparison of values in ENF specimen width for *a*=55 mm a) G_{II} values b) G_{II} /G values

3.2.3 Effect of the stacking sequence on G_{III}

The comparison of G_{III} values across the width of ENF specimens for initial crack lengths *a*=35 mm, *a*=40 mm, *a*=45 mm, *a*=50 mm, and *a*=55mm is presented in Figure 21. The results showed that the values of G_{III} in the middle part of all the specimens were zero, but at the edges of the beam, with the change of the stacking sequence, the values of the strain energy release rate in the specimen changed according to the mentioned curves, the value of the energy release rate in the state of *S4* is the highest energy release rate has been calculated and therefore the tendency of delamination in the stacking sequence of *S4* increases.

3.3 Effect of the stacking sequence on G values in ENF specimens with fixed initial crack length

The comparison of the resistance curves in the middle of the ENF specimen for the different stacking sequences of S1, S2, S3, and S4 is presented in Figure 22. By changing the stacking sequence, the strain energy release rate values varied among the investigated laminates. For the S1, S3, and S4 configurations, the strain energy release rate increased with increasing initial crack length. However, the S2 configuration exhibited different behavior at *a* = 55 mm, with a reduction in the calculated strain energy release rate relative to the overall trend. This behavior may be associated with the interaction between laminate stacking sequence, stiffness coupling effects, and the adopted numerical assumptions. Further investigation is required to determine the underlying mechanism and assess the potential influence of numerical factors.

4. Conclusion

In this article, 20 specimens, each with a different stacking sequence and varying initial crack lengths have been modeled in Abaqus, and it was observed that under identical conditions, susceptibility to delamination increases with the increase in initial crack length, along with variation of G_I, G_{II}, and G_{III} within the specimen width. Aside from local edge effects, distributions are rather uniform. The other result showed that mode II is always dominant, and in the case of the ENF specimen, the mean value of the contribution of mode II to the whole strain energy release rate $G = G_I + G_{II} + G_{III}$ is above 99%. Also, by comparing different specimens, the following results were obtained.

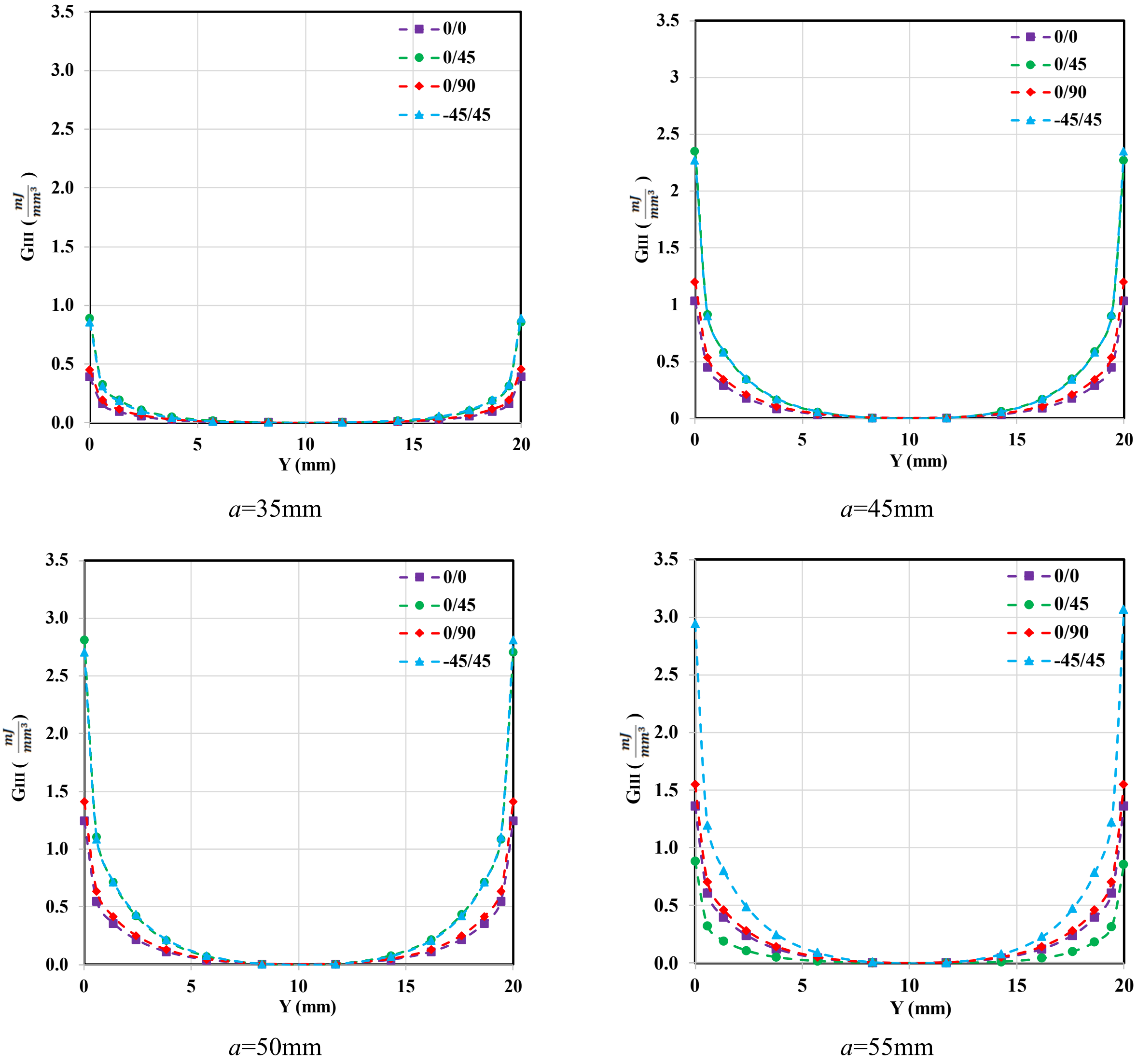

Fig. 21: Comparison of G_{III} values in ENF specimen width with fixed initial crack length

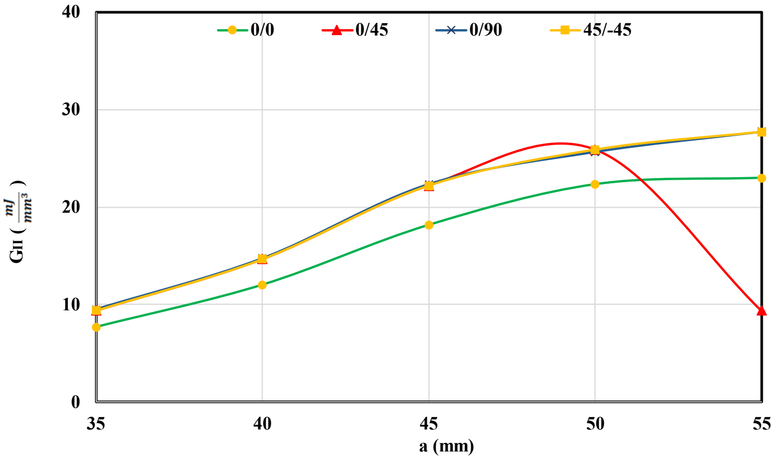

Fig. 22: Resistance curve (R curve) of ENF specimen

- A comparison of the G_I values across the width of the ENF specimen for all different stacking sequences also revealed different initial crack length values, which in most of the cases would be zero and in some cases the value would be equivalent to G_I and the value would be so small (e-12) that it can be considered to be zero.
- The comparison of G_{II} values across the width of the ENF specimen for each stacking sequence showed that

with the increase in the length of the initial crack, the values of the strain energy release rate in the specimen increase, and therefore the susceptibility of delamination increases in cases where the length of the initial crack is longer. Also, by changing the stacking sequence, the strain energy release rate in the specimen changes. The value of the energy release rate is the lowest in *S1,* and with the asymmetry of the stacking sequence of *S2* and *S3,* or the angulation of the fibers (*S4*), the available G_{II} values increased, and therefore, the susceptibility of delamination increases in these cases. This behavior can be explained by the interlaminar stress distribution ahead of the crack tip. In the symmetric *S1* laminate, more uniform bending reduces interlaminar shear and normal stress concentrations, resulting in lower ERR values. In contrast, the asymmetric configurations (*S2* and *S3*) introduce stronger stiffness mismatch and bending-coupling effects, which increase local crack-tip stresses. The *S4* configuration, due to its larger fiber-angle mismatch, generates the highest local interlaminar stress concentration and therefore the highest fracture driving force.

- The comparison of G_{III} values across the width of the ENF specimen for each stacking sequence showed that the G_{III} values in the middle part of all specimens were zero, but at the edges of the beam, with the increase in the length of the initial crack, the values of the strain energy release rate in the specimen increased, and therefore the driving force for delamination in cases where the initial crack length is longer and increases at the edges. Also, by changing the stacking sequence (taking into account the fixed initial crack length), the value of the energy release rate has been calculated to be the highest in *S4,* and therefore, the tendency of separation of plies in the stacking sequence of *S4* increases.
- The strain energy release rate values varied with the stacking sequence. For the *S1*, *S3*, and *S4* laminates, the strain energy release rate increased with increasing initial crack length. However, the *S2* configuration exhibited a different trend at a = 55 mm, where a reduction in the calculated strain energy release rate was observed compared with the overall trend. Further investigation is required to determine the underlying mechanism of this behavior.

It should be noted that the distributions of GI, GII and GIII and the observation of the effect of crack length and stacking sequence on the strain energy release rate are directly derived from the present 3-D finite element analyses. These numerical results have been interpreted as per the following: the delamination susceptibility, fracture driving force and laminate performance are interpreted in the context of the following assumptions used in the model: linear elastic material behavior, VCCT-based fracture analysis and the specific laminate configuration used in this study.

Experimental validation and progressive damage modeling of mixed-mode delamination behavior in composite laminates with different stacking sequences and crack lengths should be carried out in the future to investigate the effect of stacking sequence and crack length on the delamination behavior further.

Nomenclature

ENF: End-Notched Flexure
VCCT: Virtual Crack Closure Technique
FE: Finite Element
ERR: Strain Energy Release Rate
LEFM: Linear Elastic Fracture Mechanics
BK: Benzeggagh–Kenane criterion
G_I: Mode I strain energy release rate (opening mode)
G_{II}: Mode II strain energy release rate (sliding mode)
G_{III}: Mode III strain energy release rate (tearing mode)
G: Total strain energy release rate ($G_I + G_{II} + G_{III}$)
$\mathbf{G_{I_c}}$: Critical Mode I fracture toughness
$\mathbf{G_{II_c}}$: Critical Mode II fracture toughness
$\mathbf{G_{III_c}}$: Critical Mode III fracture toughness
Δa: Virtual crack extension length
a: Initial crack length
b: Specimen width
h: Half laminate thickness
$\mathbf{D_c}$: Bending stiffness parameter
S1–S4: Laminate stacking sequence configurations
U1, U2, U3: Displacement components along global directions
S12: In-plane shear stress
S22: Normal stress in the 2-direction

Disclosure statement

No potential conflict of interest was reported by the authors.

Funding

We would like to clarify that this research received no external funding from any organization or agency.

References

[1] Sabbaghian M, Kheyroddin A. Flexural strengthening of RC one way slabs with high-performance fiber-reinforced cementitious composite laminates using steel and GFRP bar. Eng Struct 2020;221:111106. https://doi.org/10.1016/J.ENGSTRUCT.2020.111106.

[2] Sabbaghian M, Kheyroddin A. Experimental investigation of shear behavior of one- way reinforced slabs with high-performance fiber- reinforced cementitious composite laminates. Amirkabir Journal of Civil Engineering 2022;53:919–22. https://doi.org/10.22060/CEEJ.2020.18138.6778.

[3] Zubillaga L, Turon A, Renart J, Costa J LP. An experimental study on matrix crack induced delamination in composite laminates. Compos Struct 2015;127:10–7.

[4] Gong W, Chen J PEA. An experimental study of the behaviour of delaminations in composite panels subjected to bending. Compos Struct 2015;123:9–18.

[5] Mishra PK, Pradhan AK, Pandit MK. Inter-laminar delamination analyses of Spar Wingskin Joints made with flat FRP composite laminates. Int J Adhes Adhes 2016;68:19–29. https://doi.org/10.1016/J.IJADHADH.2016.02.001.

[6] Shokrieh MM, Heidari-Rarani M, Ayatollahi MR. Delamination R-curve as a material property of unidirectional glass/epoxy composites. Mater Des 2012;34:211–8. https://doi.org/10.1016/J.MATDES.2011.08.006.

[7] de Morais AB, Pereira AB. Mixed mode I + II interlaminar fracture of glass/epoxy multidirectional laminates – Part 1: Analysis. Compos Sci Technol 2006;66:1889–95. https://doi.org/10.1016/J.compositech.2006.04.006.

[8] de Morais AB, Pereira AB. Mixed mode II + III interlaminar fracture of carbon/epoxy laminates. Compos Sci Technol 2008;68:2022–7. https://doi.org/10.1016/J.COMPSCITECH.2008.02.023.

[9] Pereira AB, de Morais AB. Mixed mode I + II interlaminar fracture of glass/epoxy multidirectional laminates – Part 2: Experiments. Compos Sci Technol 2006;66:1896–902. https://doi.org/10.1016/J.COMPSCITECH.2006.04.008.

[10] Standard test method for mode I interlaminar fracture toughness of unidirectional fiber-reinforced polymer matrix composites . n.d.

[11] Test Method for Determination of the Mode II Interlaminar Fracture Toughness of Unidirectional Fiber-Reinforced Polymer Matrix Composites 2019. https://doi.org/10.1520/D7905_D7905M-19E01.

[12] Tsai SW, Hahn HT. Introduction to Composite Materials. Introduction to Composite Materials 2018. https://doi.org/10.1201/9780203750148.

[13] Bascom WD, Bitner JL, Moulton RJ, Siebert AR. The interlaminar fracture of organic-matrix, woven reinforcement composites. Composites 1980;11:9–18. https://doi.org/10.1016/0010-4361(80)90016-6.

[14] Wood MDK, Sun X, Tong L, Luo Q, Katzos A, Rispler A. A new ENF test specimen for the mode II delamination toughness testing of stitched woven CFRP laminates. J Compos Mater 2016;41:1743–72. https://doi.org/10.1177/0021998306069890.

[15] Alif N, Carlsson LA, Gillespie JW. Mode I, Mode II, and Mixed Mode Interlaminar Fracture of Woven Fabric Carbon/Epoxy. ASTM Special Technical Publication 1997;1242:82–106. https://doi.org/10.1520/STP18271S.

[16] Pereira AB, De Morais AB. Mode II interlaminar fracture of glass/epoxy multidirectional laminates. Compos Part A Appl Sci Manuf 2004;35:265–72. https://doi.org/10.1016/J.COMPOSITESA.2003.09.028.

[17] Triki E, Zouari B, Dammak F. Dependence of the interlaminar fracture toughness of E-Glass/Polyester woven fabric composites laminates on ply orientation. Eng Fract Mech 2016;159:63–78. https://doi.org/10.1016/J.ENGFRACMECH.2016.03.025.

[18] Gliszczynski A, Wiącek N. Experimental and numerical benchmark study of mode II interlaminar fracture toughness of unidirectional GFRP laminates under shear loading using the end-notched flexure (ENF) test. Compos Struct 2021;258:113190. https://doi.org/10.1016/J.COMPSTRUCT.2020.113190.

[19] Gong Y, Xia K, Wang Y, Zhao L, Zhang J, Hu N. A semi-analytical model for the mode II fracture toughness of multidirectional composite laminates. Thin-Walled Structures 2023;182:110235. https://doi.org/10.1016/J.TWS.2022.110235.

[20] Tu W, Pascoe JA, Alderliesten R. Comparison of mode II delamination behaviours in multidirectional and unidirectional composite laminates. Compos B Eng 2025;291:111941. https://doi.org/10.1016/J.COMPOSITESB.2024.111941.

[21] Choi NS, Kinloch AJ WJG. Delamination fracture of multidirectional carbon-fiber/epoxy composites under mode I, mode II and mixed-mode I/II loading. J Compos Mater 1999;33:73–100.

[22] Polaha JJ, Davidson BD, Hudson RC PA. Effects of mode ratio, ply orientation and precracking on the delamination toughness of a laminated composite. J Reinforced Plast Compos 1996;15:141–73.

[23] Hwang JH, Lee CS, Hwang W. Effect of crack propagation directions on the interlaminar fracture toughness of carbon/epoxy composite materials. Applied Composite Materials 2001 8:6 2001;8:411–33. https://doi.org/10.1023/A:1012663722334.

[24] Hwang JH, Kwon O, Lee CS, Hwang W. Interlaminar fracture and low-velocity impact of carbon/epoxy composite materials. Mechanics of Composite Materials 2000 36:2 2000;36:117–30. https://doi.org/10.1007/BF02681828.

[25] Moustapha Sarr M, Kosaka T. Effect of cellulose nanofibers on the fracture toughness mode II of glass fiber/epoxy composite laminates. Heliyon 2023;9:e13203. https://doi.org/10.1016/J.HELIYON.2023.E13203.

[26] Syed Abdullah SIB, Bokti SK, Wong KJ, Johar M, Chong WWF, Dong Y. Mode II and mode III delamination of carbon fiber/epoxy composite laminates subjected to a four-point bending mechanism. Compos B Eng 2024;270:111110. https://doi.org/10.1016/J.COMPOSITESB.2023.111110.

[27] Gfrerrer M, Koss V, Wiener J, Schuecker C, Brunner AJ, Pinter G. Comparing Mode I, Mode II and Mixed-Mode I/II interlaminar fracture toughness of glass and carbon fiber reinforced polymer laminates with the same epoxy matrix system. Eng Fract Mech 2025;320:111009. https://doi.org/10.1016/J.ENGFRACMECH.2025.111009.

[28] Ever J. Barbero. Finite Element Analysis of Composite Materials Using Abaqus. Taylor & Francis Group; 2013.

[29] Shahverdi M, Vassilopoulos, Anastasios P, Keller T. Mixed-mode I/II fracture behavior of asymmetric adhesively-bonded pultruded composite joints. Eng Fract Mech 2013.

[30] Valvo PS. A physically consistent virtual crack closure technique for I/II/III mixed-mode fracture problems. Procedia Materials Science 2014;3:1983–7. https://doi.org/10.1016/J.MSPRO.2014.06.319.

[31] Valvo PS. On the calculation of energy release rate and mode mixity in delaminated laminated beams. Eng Fract Mech 2016;165:114–39. https://doi.org/10.1016/J.ENGFRACMECH.2016.08.010.

[32] Reeder J, Song K, Chunchu P, Ambur D. Postbuckling and Growth of Delaminations in Composite Plates Subjected to Axial Compression 2002. https://doi.org/10.2514/6.2002-1746.

[33] Rice JR. A Path Independent Integral and the Approximate Analysis of Strain Concentration by Notches and Cracks. J Appl Mech 1968;35:379–86. https://doi.org/10.1115/1.3601206.

[34] Benzeggagh ML, Kenane M. Measurement of mixed-mode delamination fracture toughness of unidirectional glass/epoxy composites with mixed-mode bending apparatus. Compos Sci Technol 1996;56:439–49. https://doi.org/10.1016/0266-3538(96)00005-X.

[35] Barbero EJ, Reddy JN. Jacobian derivative method for three-dimensional fracture mechanics. Communications in Applied Numerical Methods 1990;6:507–18. https://doi.org/10.1002/CNM.1630060703;WGROUP:STRING:PUBLICATION.

[36] Ozdil F, Carlsson LA DP. Beam analysis of angle-ply laminate end-notched flexure specimens. Compos Sci Technol 1998;58:1929–38.

[37] Davidson BD, Kru¨ger R KM. Three dimensional analysis and resulting design recommendations for unidirectional and multidirectional end-notched flexure tests. J Compos Mater 1995;29:2108–33.

[38] Tao J, Sun CT. Influence of ply orientation on delamination in composite laminates. J Compos Mater 1998;32:1933–47. https://doi.org/10.1177/002199839803202103;CTYPE:STRING:JOURNAL.

[39] Chow WT AS. Stress intensity factors as the fracture parameters for delamination crack growth in composite laminates. Composites 1997;28:375–84.

[40] Raju IS, Crews JH AMA. Convergence of strain energy release rate components for edge delaminated composite laminates. Engng Fract Mech 1988;30:383–96.

[41] Narayan SH BJL. Designation of mode mix in orthotropic composite delamination problems. Int J Fract 1998;90:383–400.

[42] Test Method for Determination of the Mode II Interlaminar Fracture Toughness of Unidirectional Fiber-Reinforced Polymer Matrix Composites 2019. https://doi.org/10.1520/D7905_D7905M-19E01.

[43] Samborski S. Analysis of the end-notched flexure test configuration applicability for mechanically coupled fiber reinforced composite laminates. Compos Struct 2017;163:342–9. https://doi.org/10.1016/J.COMPSTRUCT.2016.12.051.